Sokolov, Maksim; Saarakkala, Seppo E.; Hosseinzadeh, Reza; Hinkkanen, Marko

Modeling of a bearingless flux-switching permanent-magnet linear motor

Published in:
Proceedings of the 2018 IEEE Transportation Electrification Conference and Expo, ITEC 2018

DOI:
10.1109/ITEC.2018.8450190

Published: 13/06/2018

Document Version
Peer-reviewed accepted author manuscript, also known as Final accepted manuscript or Post-print

Please cite the original version:
Sokolov, M., Saarakkala, S. E., Hosseinzadeh, R., & Hinkkanen, M. (2018). Modeling of a bearingless flux-switching permanent-magnet linear motor. In *Proceedings of the 2018 IEEE Transportation Electrification Conference and Expo, ITEC 2018* (pp. 851-857). (IEEE transportation electrification conference and expo). IEEE. https://doi.org/10.1109/ITEC.2018.8450190

Modeling of a Bearingless Flux-Switching Permanent-Magnet Linear Motor

Maksim Sokolov, Seppo E. Saarakkala, Reza Hosseinzadeh, and Marko Hinkkanen

Aalto University School of Electrical Engineering, P.O. Box 15500, FI-00076 Aalto, Finland

***Abstract*—This paper deals with dynamic modeling of a bearingless flux-switching permanent-magnet (FSPM) linear machine. Based on equivalent magnetic models, an analytical model is derived, taking into account airgap variation and magnetic saturation. The effects of these phenomena are analyzed using finite-element method (FEM) simulations of a test motor. The proposed model can be fitted to the FEM data or measured data. The model can be applied in real-time control of a magnetically levitating motor drive as well as in time-domain simulations. Experimental results are used to validate the proposed model.**

I. Introduction

A rotating flux-switching permanent-magnet (FSPM) machine has a very simple rotor structure, due to its permanent magnets (PMs) and three-phase concentrated winding being located in the stator [1], [2]. This machine type has comparatively high power density. Its back-emf phase voltages are almost sinusoidal. A typical configuration has 12 stator teeth and 10 rotor poles (12/10). Recently, a bearingless version of an FSPM machine has been developed [3]. In addition to torque production, bearingless motors also produce a radial force, which can be controlled to allow for a contactless operation of the machine. Usually a multiphase winding structure is used in bearingless FSPM machines to produce an uneven flux density in the airgap, which creates an unbalanced magnetic pull on the rotor.

Linear variants of FSPM machines [4] have become an interesting option for producing the thrust force in various applications, such as traction [5], wave-energy generation [6], urban rail transit [7], electromagnetic launch systems [8] and elevator systems [9]. One of the most important benefits of using an FSPM machine type as a linear motor is in having both magnets and windings in the same part of the motor. Hence, in traction applications, the rail or track along which the motor travels can be made without using any active materials apart from iron, which significantly reduces the costs. Like their rotating counterparts, FSPM linear machines can be modeled and controlled using two-axis models [7]. Various analytical and semi-analytical models have been presented for machine design and analysis purposes [10], [11].

In addition to the thrust force, linear FSPM machines also produce a normal force component that pulls the mover towards the rail. Since this attraction force is large, these machines typically have a double-sided or four-sided structure [6] in order to balance the magnetic pull on both sides of the rail. A bearingless version of an FSPM linear motor can be created by actively controlling the attraction force to maintain a constant airgap.

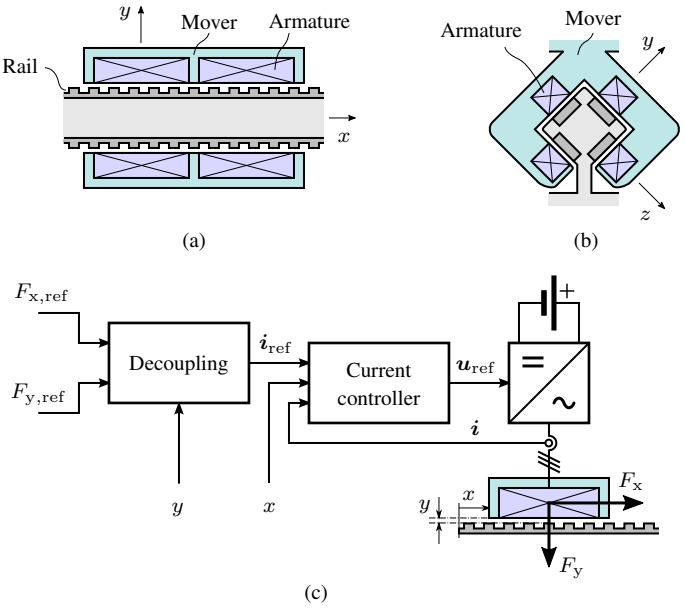

Fig. 1. Example configuration of a bearingless linear motor system, consisting of a beam with rails and a mover with eight motor units: (a) cross-section in the xy plane; (b) cross-section in the yz plane; (c) decoupled force controller for a single motor unit. The thrust-force reference $F_{\mathrm{x,ref}}$ is obtained from the traction controller and the normal-force reference $F_{\mathrm{y,ref}}$ from the levitation controller.

A magnetically levitating linear motor drive system may consist of bearingless FSPM linear motor drive units. The motor units can be arranged in various ways such that linear motion is produced and remaining degrees of freedom are stabilized. Figs. 1(a) and (b) illustrate an example configuration. Motion in the x direction is produced and the remaining five degrees of freedom are stabilized. Similar configurations have been considered with mechanical bearings, e.g. [6], [9].

The need of an active magnetic levitation in the bearingless drive system presents a challenge from the control point of view, since the system is inherently unstable and nonlinear due to magnetic saturation and varying airgap. Therefore, knowing the analytical magnetic model of the system is beneficial, e.g., when designing a model-based current controller, decoupling the force production in the x and y directions, and linearizing the highly non-linear system, cf. Fig. 1(c). Furtermore, the analytical model can be applied, e.g., in stability analysis and

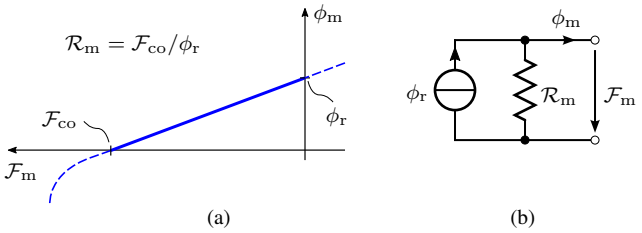

Fig. 2. PM model: (a) demagnetization curve; (b) Norton equivalent model.

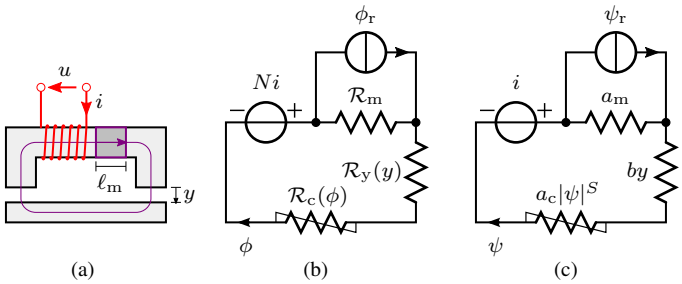

Fig. 3. Preliminary example: (a) electromagnet including the coil and the PM; (b) equivalent magnetic model using fluxes and mmfs; (c) equivalent magnetic model using flux linkages and currents.

in time-domain simulations.

This paper deals with dynamic modeling of a bearingless FSPM linear machine for purposes of control design and real-time implementation. The main contributions of this paper can be summarized as follows:

1) Analytical equations describing the magnetic model and force production are derived.
2) Using the FEM, the magnetic characteristics of the machine are analyzed, including magnetic saturation and the influence of the airgap variation.
3) A simple method for estimating the model parameters from the FEM or measured data is presented.

Experimental results are used to validate the proposed model.

II. Preliminaries

A. Modeling of a PM

The demagnetization curve of the PM in the second quadrant is approximated with a straight line according to Fig. 2(a). The Norton equivalent model is used to represent the effect of PMs, cf. Fig. 2(b). The magnetomotive force (mmf) of the PM is $\mathcal{F}_\mathrm{m} = \mathcal{R}_\mathrm{m}(\phi_\mathrm{r} - \phi_\mathrm{m})$, where the remanent flux ϕ_r is constant. The internal reluctance is

$$\mathcal{R}_\mathrm{m} = \frac{\ell_\mathrm{m}}{\mu_0 A_\mathrm{m}} \tag{1}$$

where ℓ_m is the width and A_m is the cross-section area of the PM.

B. Modeling of Magnetic Saturation

The mmf in the saturated core is $\mathcal{F}_\mathrm{c} = \mathcal{R}_\mathrm{c}(\phi_\mathrm{c})\phi_\mathrm{c}$, where ϕ_c is the magnetic flux in the core. In accordance with [12], the nonlinear reluctance is modeled as[1]

$$\mathcal{R}_\mathrm{c}(\phi) = \frac{\ell_\mathrm{c}}{\mu_0 A_\mathrm{c}} a_\mathrm{c}' |\phi_\mathrm{c}|^S \tag{2}$$

where ℓ_c is the length of the flux path in the core, A_c is the cross-section area of the core, and a_c' and S are positive constants. The exponent S determines the shape of the saturation characteristics.

[1]The constant term included in [12] is dropped here, but it will be effectively taken into account via other reluctances in the following equivalent models.

C. Example: Electromagnet With Saturable Core

Consider an electromagnet shown in Fig. 3. The system consists of the core, the PM, and the coil having N turns. The coil is fed by the current i, leading to the mmf Ni. The fringing and leakage fluxes are omitted. The flux densities in the airgap, in the PM, and in the core are assumed to be uniform. The total reluctance of the two airgaps is

$$\mathcal{R}_\mathrm{y}(y) = \frac{2y}{\mu_0 A_\mathrm{y}} \tag{3}$$

where y is width of the airgap and A_y is the cross-section area of the airgap. Based on Figs. 3(b) and 3(c), the coil current is

$$\begin{aligned} i &= \frac{(\mathcal{R}_\mathrm{m} + \mathcal{R}_\mathrm{y} + \mathcal{R}_\mathrm{c})\psi - \mathcal{R}_\mathrm{m}\psi_\mathrm{r}}{N^2} \\ &= \left(a_\mathrm{m} + by + a_\mathrm{c}|\psi|^S\right)\psi - a_\mathrm{m}\psi_\mathrm{r} \end{aligned} \tag{4}$$

where $\psi = N\phi$ is the coil flux linkage and $\psi_\mathrm{r} = N\phi_\mathrm{r}$ is constant. In the last form, a_m, b, and a_c are geometry-dependent constants. If needed, these constants could be easily derived based on the given equations and assumptions. It is worth noticing that $1/a_\mathrm{m}$ equals the unsaturated inductance at $y = 0$.

The coupling magnetic field is assumed to be lossless [13]. The rate of change of the field energy is

$$\frac{\mathrm{d}W}{\mathrm{d}t} = i\frac{\mathrm{d}\psi}{\mathrm{d}t} - F_\mathrm{y}\frac{\mathrm{d}y}{\mathrm{d}t} \tag{5}$$

Using (4), the field energy can be integrated

$$W = \frac{a_\mathrm{m}(\psi - \psi_\mathrm{r})^2}{2} + \frac{by\psi^2}{2} + \frac{a_\mathrm{c}|\psi|^{S+2}}{S+2} \tag{6}$$

and the expression for the attractive force can be derived

$$F_\mathrm{y} = -\frac{\partial W}{\partial y} = -\frac{b\psi^2}{2} \tag{7}$$

The same modeling principles will be used in the following for the FSPM linear machine.

III. Modeling of an FSPM Linear Motor

A three-phase bearingless FSPM linear motor, consisting of a rail and a mover, is considered. The rail is composed of electric steel sheets and it is toothed. The mover includes both the PMs and a three-phase winding. Since the three-phase winding is either delta-connected or the star point is not

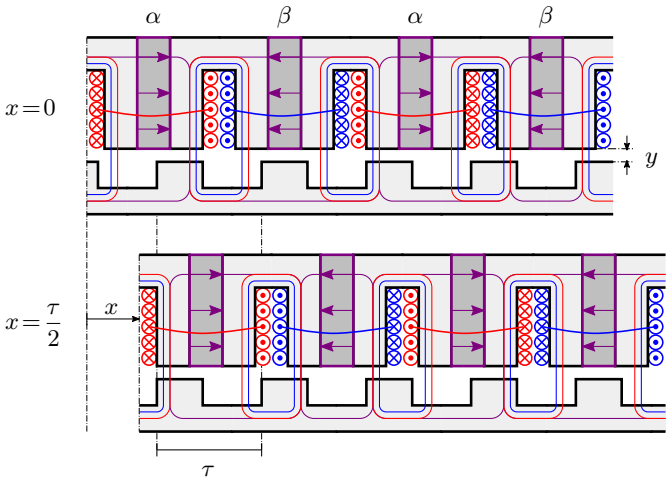

Fig. 4. Conceptual two-phase FSPM linear motor, corresponding to the 4-slot/5-pole configuration. The magnets are placed between the coils and their polarities are shown by the arrows. The crosses and dots define the positive direction of the coil currents. The phases α and β are labeled above the corresponding coils. The most significant flux paths due to the PMs (purple), d-axis winding (red), and q-axis widing (blue) are also sketched.

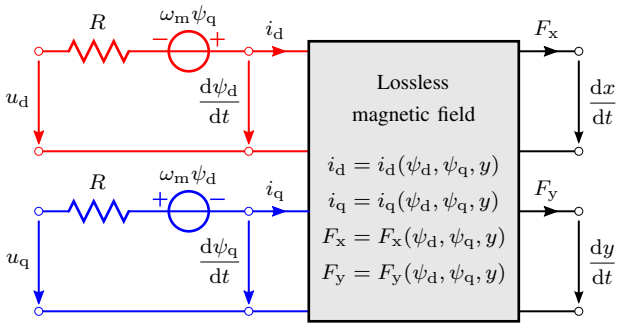

Fig. 5. Dynamic model in dq coordinates, rotating at $\omega_\mathrm{m} = (2\pi/\tau) \cdot \mathrm{d}x/\mathrm{d}t$.

connected, the zero-sequence current cannot flow. Therefore, the zero-sequence components cannot contribute the power or forces and an equivalent two-phase $\alpha\beta$ model can be used. Using the phase currents i_a, i_b, and i_c as an example, the $\alpha\beta$ components are obtained as

$$\begin{bmatrix} i_\alpha \\ i_\beta \end{bmatrix} = \frac{2}{3} \begin{bmatrix} 1 & -1/2 & -1/2 \\ 0 & \sqrt{3}/2 & -\sqrt{3}/2 \end{bmatrix} \begin{bmatrix} i_\mathrm{a} \\ i_\mathrm{b} \\ i_\mathrm{c} \end{bmatrix} \tag{8}$$

The same transformation applies for the flux linkages and the voltages.

A. Conceptual Two-Phase Model

Fig. 4 illustrates a conceptual two-phase FSPM linear motor, corresponding to the simple 4-slot/5-pole configuration. This conceptual model includes essentially the same phenomena, which are encountered in more complex three-phase configurations. The dominant flux paths are sketched in the figure. When the mover is positioned at $x = 0$, the PM flux linking with the α-phase coils has its maximum value. It can be seen that the polarity of the α-phase flux linkage is reversed, as the

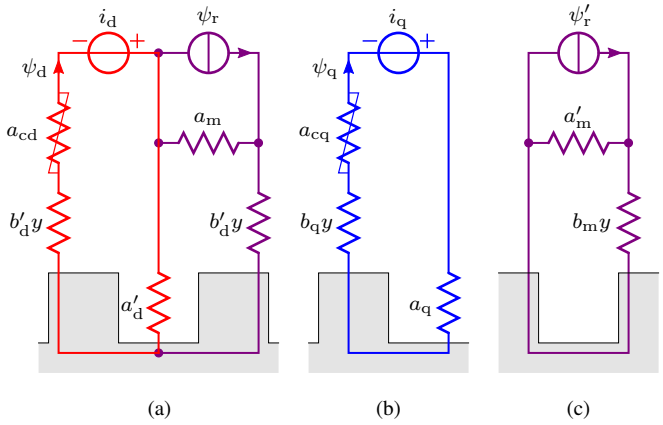

Fig. 6. Simplified equivalent magnetic model: (a) d-axis winding; (b) q-axis winding; (c) PM flux crossing the airgap but not linking with the windings.

mover moves from $x = 0$ to $x = \tau/2$, where τ is the pole pitch of the rail. In well designed machines, the flux linkages vary almost sinusoidally as function of the position x.

There are also leakage fluxes in the motor, especially at the both ends of the PMs. The leakage fluxes (in the airgap-side of the PMs) as well as the fringing fluxes depend on the airgap length y and affect the normal-force production. The leakage and fringing fluxes are not explicitly modeled, but their effects are indirectly included in the model via the parameter fitting procedure. The end effects are omitted in this paper.

B. Dynamic Model in Rail Coordinates

Fig. 5 shows the lumped-element dynamic model of the motor in in rail (dq) coordinates. As an example, the dq components of the current are

$$\begin{bmatrix} i_\mathrm{d} \\ i_\mathrm{q} \end{bmatrix} = \begin{bmatrix} \cos(\vartheta_\mathrm{m}) & \sin(\vartheta_\mathrm{m}) \\ -\sin(\vartheta_\mathrm{m}) & \cos(\vartheta_\mathrm{m}) \end{bmatrix} \begin{bmatrix} i_\alpha \\ i_\beta \end{bmatrix} \tag{9}$$

where the position x of the mover with respect to the rail is expressed in radians as $\vartheta_\mathrm{m} = 2\pi x/\tau$. The d-axis is aligned so that the flux linkage due to the PMs has its maximum value in the α-phase at $\vartheta_\mathrm{m} = 0$. The voltage equations in rail coordinates are

$$\frac{\mathrm{d}\psi_\mathrm{d}}{\mathrm{d}t} = u_\mathrm{d} - Ri_\mathrm{d} + \omega_\mathrm{m}\psi_\mathrm{q} \tag{10a}$$

$$\frac{\mathrm{d}\psi_\mathrm{q}}{\mathrm{d}t} = u_\mathrm{q} - Ri_\mathrm{q} - \omega_\mathrm{m}\psi_\mathrm{d} \tag{10b}$$

where u_d, u_q are the voltage components, ψ_d, ψ_q are the flux-linkage components, R is the resistance, and $\omega_\mathrm{m} = (2\pi/\tau) \cdot \mathrm{d}x/\mathrm{d}t$ is the electrical angular speed.

The magnetic model can be characterized by current functions $i_\mathrm{d} = i_\mathrm{d}(\psi_\mathrm{d}, \psi_\mathrm{q}, y)$ and $i_\mathrm{q} = i_\mathrm{q}(\psi_\mathrm{d}, \psi_\mathrm{q}, y)$. The currents depend on the airgap y, which can change in bearingless motors. If spatial harmonics were taken into account, the current functions would depend on the position x as well. For finding a suitable form of these functions, equivalent magnetic models will be considered in the following.

C. Equivalent Magnetic Models

Based on the dominant flux paths in Fig. 4, simplified magnetic models in Fig. 6 can be drawn. It is easiest to start with the model for the q-axis winding shown in Fig. 6(b), yielding the q-axis current

$$i_\mathrm{q} = \left[a_\mathrm{q} + b_\mathrm{q} y + a_\mathrm{cq}(\psi_\mathrm{d}, \psi_\mathrm{q})\right] \psi_\mathrm{q} \tag{11}$$

It can be seen that the q-axis flux is assumed to travel through one rail pole. The constant a_q models the larger reluctance between the poles, while the constant b_q takes into account the reluctance due to the changing airgap y. The nonlinear element a_cq models the saturation in the mover teeth.

The d-axis model shown in Fig. 6(a) includes an analogous flux path as the q-axis model. Furthermore, the PM flux is coupled with the d-axis winding. The PM is placed in parallel with the mmf of the d-axis winding [2]. The d-axis current can be solved

$$\begin{aligned} i_\mathrm{d} = {} & \left[b'_\mathrm{d} y + a_\mathrm{cd}(\psi_\mathrm{d}, \psi_\mathrm{q})\right] \psi_\mathrm{d} \\ & + \frac{a'_\mathrm{d} a_\mathrm{m} (\psi_\mathrm{d} - \psi_\mathrm{r}) + a'_\mathrm{d} b'_\mathrm{d} y \psi_\mathrm{d}}{a'_\mathrm{d} + a_\mathrm{m} + b'_\mathrm{d} y} \end{aligned} \tag{12}$$

The airgap length appears also in the denominator in the last term. In order to simplify the model and its parameter estimation, the last term can be approximated using its series expansion at $y = 0$, leading to[2]

$$i_\mathrm{d} = \left[a_\mathrm{d} + b_\mathrm{d} y + a_\mathrm{cd}(\psi_\mathrm{d}, \psi_\mathrm{q})\right] \psi_\mathrm{d} - (a_\mathrm{d} - b_\mathrm{dm} y)\, \psi_\mathrm{r} \tag{13}$$

where the constants are

$$\begin{aligned} a_\mathrm{d} = \frac{a'_\mathrm{d} a_\mathrm{m}}{a'_\mathrm{d} + a_\mathrm{m}} \quad b_\mathrm{d} = \left[1 + \frac{a_\mathrm{d} a'_\mathrm{d}}{(a'_\mathrm{d} + a_\mathrm{m}) a_\mathrm{m}}\right] b'_\mathrm{d} \\ b_\mathrm{dm} = \frac{a_\mathrm{d} b'_\mathrm{d}}{a'_\mathrm{d} + a_\mathrm{m}} \end{aligned} \tag{14}$$

The self-axis saturation is modeled similarly to (2). Furthermore, the cross-saturation phenomenon between the d-axis and the q-axis is also taken into account [14]

$$a_\mathrm{cd} = a_\mathrm{dd} |\psi_\mathrm{d}|^S + \frac{a_\mathrm{dq}}{V+2} |\psi_\mathrm{d}|^U |\psi_\mathrm{q}|^{V+2} \tag{15a}$$

$$a_\mathrm{cq} = a_\mathrm{qq} |\psi_\mathrm{q}|^T + \frac{a_\mathrm{dq}}{U+2} |\psi_\mathrm{d}|^{U+2} |\psi_\mathrm{q}|^V \tag{15b}$$

where a_dd, a_qq, a_dq, S, T, U, V are positive constants. The terms including a_dq take the cross-saturation into account, such that the reciprocity condition $\partial i_\mathrm{d}/\partial \psi_\mathrm{q} = \partial i_\mathrm{q}/\partial \psi_\mathrm{d}$ holds. The equations (11), (13), and (15) can be collected together

$$\begin{aligned} i_\mathrm{d} = {} & \left(a_\mathrm{d} + b_\mathrm{d} y + a_\mathrm{dd} |\psi_\mathrm{d}|^S + \frac{a_\mathrm{dq}}{V+2} |\psi_\mathrm{d}|^U |\psi_\mathrm{q}|^{V+2}\right) \psi_\mathrm{d} \\ & - (a_\mathrm{d} - b_\mathrm{dm} y)\, \psi_\mathrm{r} \end{aligned} \tag{16a}$$

$$i_\mathrm{q} = \left(a_\mathrm{q} + b_\mathrm{q} y + a_\mathrm{qq} |\psi_\mathrm{q}|^T + \frac{a_\mathrm{dq}}{U+2} |\psi_\mathrm{d}|^{U+2} |\psi_\mathrm{q}|^V\right) \psi_\mathrm{q} \tag{16b}$$

If $a_\mathrm{dd} = 0$, $a_\mathrm{qq} = 0$, and $a_\mathrm{dq} = 0$ were chosen, the model would reduce to a magnetically linear model with $L_\mathrm{d} = 1/a_\mathrm{d}$ and $L_\mathrm{q} = 1/a_\mathrm{q}$.

[2]The first two terms of the series expansion $1/(k+y) = 1/k - y/k^2 + y^2/k^3 \ldots$ are used.

As can be seen in Fig. 4, one part of the PM flux crosses the airgap but does not link with the windings. This flux is important to take into account as it contributes to the production of the normal force. The flux path is assumed to have no cross-coupling and its saturation is omitted, cf. Fig. 6(c). The corresponding field energy is

$$w(y) = \frac{f y}{1 + c y} \tag{17}$$

where f and c are positive constants. It is to be noted that saturation effects may couple the leakage flux with the windings, but this coupling is quite weak and is omitted here for simplicity.

D. Forces

In accordance with Fig. 5, the rate of change of the magnetic field energy is

$$\begin{aligned} \frac{\mathrm{d}W}{\mathrm{d}t} = {} & \frac{3}{2}\left(i_\mathrm{d} \frac{\mathrm{d}\psi_\mathrm{d}}{\mathrm{d}t} + i_\mathrm{q} \frac{\mathrm{d}\psi_\mathrm{q}}{\mathrm{d}t}\right) + \frac{3\pi}{\tau}(\psi_\mathrm{d} i_\mathrm{q} - \psi_\mathrm{q} i_\mathrm{d}) \frac{\mathrm{d}x}{\mathrm{d}t} \\ & - F_\mathrm{x} \frac{\mathrm{d}x}{\mathrm{d}t} - F_\mathrm{y} \frac{\mathrm{d}y}{\mathrm{d}t} \end{aligned} \tag{18}$$

which directly gives the expression for the thrust force F_x. Using the magnetic model (16) and (17), the total field energy W is obtained, giving the normal force $F_\mathrm{y} = -\partial W/\partial y$. The resulting force expressions are

$$F_\mathrm{x} = \frac{3\pi}{\tau}(\psi_\mathrm{d} i_\mathrm{q} - \psi_\mathrm{q} i_\mathrm{d}) \tag{19a}$$

$$\begin{aligned} F_\mathrm{y} = {} & -\frac{3}{4}\left(b_\mathrm{d} \psi_\mathrm{d}^2 + b_\mathrm{q} \psi_\mathrm{q}^2 + 2 b_\mathrm{dm} \psi_\mathrm{r} \psi_\mathrm{d} - b_\mathrm{dm} \psi_\mathrm{r}^2\right) \\ & - \frac{f}{(1 + c y)^2} \end{aligned} \tag{19b}$$

Equations (10), (16), and (19) describe the dynamic model of the bearingless FSPM linear motor.

E. Parameter Estimation

The parameters of the model depend on the motor geometry. However, the aim is not to calculate these parameters based on the dimensions of the machine, but rather estimating them using the data from the FEM or from experiments. There are different methods to fit the model parameters. As an example, one fitting procedure is briefly explained in the following.

The exponents S, T, U, V can be fixed in advance (or they can be iteratively chosen). In this case, the model (16) becomes linear in parameters and it can be reformulated as a regression model

$$\boldsymbol{i} = \boldsymbol{\varphi}^\mathrm{T} \boldsymbol{\theta} \tag{20}$$

where the regressed variable is $\boldsymbol{i} = [i_\mathrm{d}, i_\mathrm{q}]^\mathrm{T}$. The regressors and the parameter vector, respectively, are

$$\boldsymbol{\varphi} = \begin{bmatrix} \psi_\mathrm{d} & 0 \\ 0 & \psi_\mathrm{q} \\ y\psi_\mathrm{d} & 0 \\ 0 & y\psi_\mathrm{q} \\ |\psi_\mathrm{d}|^S\psi_\mathrm{d} & 0 \\ 0 & |\psi_\mathrm{q}|^T\psi_\mathrm{q} \\ \frac{|\psi_\mathrm{d}|^U|\psi_\mathrm{q}|^{V+2}\psi_\mathrm{d}}{V+2} & \frac{|\psi_\mathrm{d}|^{U+2}|\psi_\mathrm{q}|^V\psi_\mathrm{q}}{U+2} \\ -1 & 0 \\ y & 0 \end{bmatrix} \quad \boldsymbol{\theta} = \begin{bmatrix} a_\mathrm{d} \\ a_\mathrm{q} \\ b_\mathrm{d} \\ b_\mathrm{q} \\ a_\mathrm{dd} \\ a_\mathrm{qq} \\ a_\mathrm{dq} \\ i_\mathrm{m} \\ h \end{bmatrix} \tag{21}$$

The original parameters are obtained as $\psi_\mathrm{r} = i_\mathrm{m}/a_\mathrm{d}$ and $b_\mathrm{dm} = h/\psi_\mathrm{r}$. The linear least squares (LLS) method can be used to solve the parameter vector, if the data set $\{i_\mathrm{d}(n), i_\mathrm{q}(n), \psi_\mathrm{d}(n), \psi_\mathrm{q}(n), y(n)\}$, $n = 1 \ldots N$, is available. The number of samples N should be larger than the number of parameters. Thus, the parameter estimation problem reduces to solving a set of linear equations. Neither initial values nor cost functions are needed. The normal-force expression (19b) can also be reformulated as a regression model

$$\sqrt{-\frac{1}{F_\mathrm{y} + \frac{3}{4}\left(b_\mathrm{d}\psi_\mathrm{d}^2 + b_\mathrm{q}\psi_\mathrm{q}^2 + 2b_\mathrm{dm}\psi_\mathrm{r}\psi_\mathrm{d} - b_\mathrm{dm}\psi_\mathrm{r}^2\right)}} = \theta_1 + \theta_2 y \tag{22}$$

After applying the LLS method again, the remaining two unknown parameters are obtained as $f = 1/\theta_1^2$ and $c = \theta_2/\theta_1$.

IV. Results

In this section, an example test machine is analysed by means of the FEM and experiments. The current components $(i_\mathrm{d}, i_\mathrm{q})$ and the force components $(F_\mathrm{x}, F_\mathrm{y})$ of the system were solved as a function of flux linkages and airgap $(\psi_\mathrm{d}, \psi_\mathrm{q}, y)$ in predefined operating points using the static FEM [15]. The operating points were chosen to cover the whole operating range of the machine in terms of allowable currents and possible airgap variation.

The results of the FEM computation were used for estimating the parameters of the proposed model as described in Section III-E. The exponents $S = T = 2$ and $U = V = 0$ were selected. Table I shows three cases, fitted using the same FEM data. In Case 1, all the modeled phenomena are included in the model. In Case 2, the magnetic saturation is ignored. In Case 3, the PMs and the d-axis winding are assumed to be in series (i.e., $a_\mathrm{d}' = \infty$ giving $b_\mathrm{dm} = 0$).

TABLE I
Model Parameters With Exponents $S = T = 2$ and $U = T = 0$

Parameter	Unit	Case 1	Case 2	Case 3
ψ_r	Vs	0.74	0.22	0.16
a_d	H^{-1}	3.60	11.1	10.6
a_q	H^{-1}	4.45	11.5	11.6
b_d	$(\mathrm{H{\cdot}m})^{-1}$	−390	−360	5.21
b_q	$(\mathrm{H{\cdot}m})^{-1}$	−361	−228	−228
b_dm	$(\mathrm{H{\cdot}m})^{-1}$	1020	3180	0
a_dd	$\mathrm{H}^{-1}\cdot(\mathrm{Vs})^{-2}$	11.1	0	0
a_qq	$\mathrm{H}^{-1}\cdot(\mathrm{Vs})^{-2}$	11.5	0	0
a_dq	$\mathrm{H}^{-1}\cdot(\mathrm{Vs})^{-2}$	21.8	0	0
f	kN	5.33	5.07	5.07
c	m^{-1}	263	302	340

A. Comparison Between the FEM Data and the Fitted Model

The fitting results are compared to the FEM data by using three-dimensional surfaces shown in Fig. 7. The flux-linkage components are plotted as function of current components and forces are plotted as function of flux-linkage components at fixed airgap values. Based on the FEM results, it was found out that both the d- and q-axes of the motor are saturating strongly. It can be seen that the fitted surfaces follow the shape of the FEM data well. Figs. 7(b), 7(c), 7(e), 7(f) show that the model is able to predict the forces also at close to zero airgap and at close to twice the nominal airgap. Naturally, some errors in the force surfaces are noticeable. However, for control purposes, it is important that the surfaces are smooth and that their shapes are predictable and physically consistent. The model was also fitted to the FEM data of another FSPM linear motor design and the fitting showed equally good results.

B. Experiments

The experimental system consists of two converter-fed FSPM motor units, which are mounted in a double-sided configuration according to Fig. 8. The mover could be levitated in the y direction by adjusting the currents of the two motor units. However, for the purposes of the force measurements, the mover was fixed into desired constant y positions using the four load cells, mounted at each corner of motor unit 1, and the differential normal force $\Delta F_\mathrm{y} = F_\mathrm{y1} - F_\mathrm{y2}$ was measured at different d-axis currents. The d-axes currents are selected to be $i_\mathrm{d1} = -i_\mathrm{d2}$ and varied between 0 and 12 A. The q-axis currents were kept at zero, $i_\mathrm{q1} = i_\mathrm{q2} = 0$.

The movement in the x direction was mechanically disabled by using a counterweight for compensating the gravitational force acting on the mover. In addition to ΔF_y, the airgap lengths y_1, y_2, and the currents of the both motor units were measured. The differential airgap is defined as $\Delta y = y_2 - y_1$. The nominal airgap of the system is 1.05 mm. Naturally, the differential airgap is zero at the nominal airgap.

Fig. 9 shows the measured forces together with the forces from the FEM and from the proposed model at three differential airgaps ($\Delta y = -0.2$ mm, $\Delta y = -0.8$ mm, and $\Delta y = -1.4$ mm). It can be seen that the results from the experiments, FEM, and model match well. The forces from the FEM data and from the model differ more from the measured forces in the case of the largest airgap. The accuracy of the proposed model should be sufficient for model-based real-time control, for example.

In order to demonstrate the importance of different modeled phenomena in the proposed model, the forces predicted by the model [corresponding to Fig. 9(a)] are shown in Fig. 10 for the magnetically linear case ($a_\mathrm{dd} = a_\mathrm{qq} = a_\mathrm{dq} = 0$) and for the case where the PMs and the d-axis winding are in series connection ($b_\mathrm{dm} = 0$). Fig. 10 demonstrates that the accuracy of the model decreases significantly, if some phenomena are

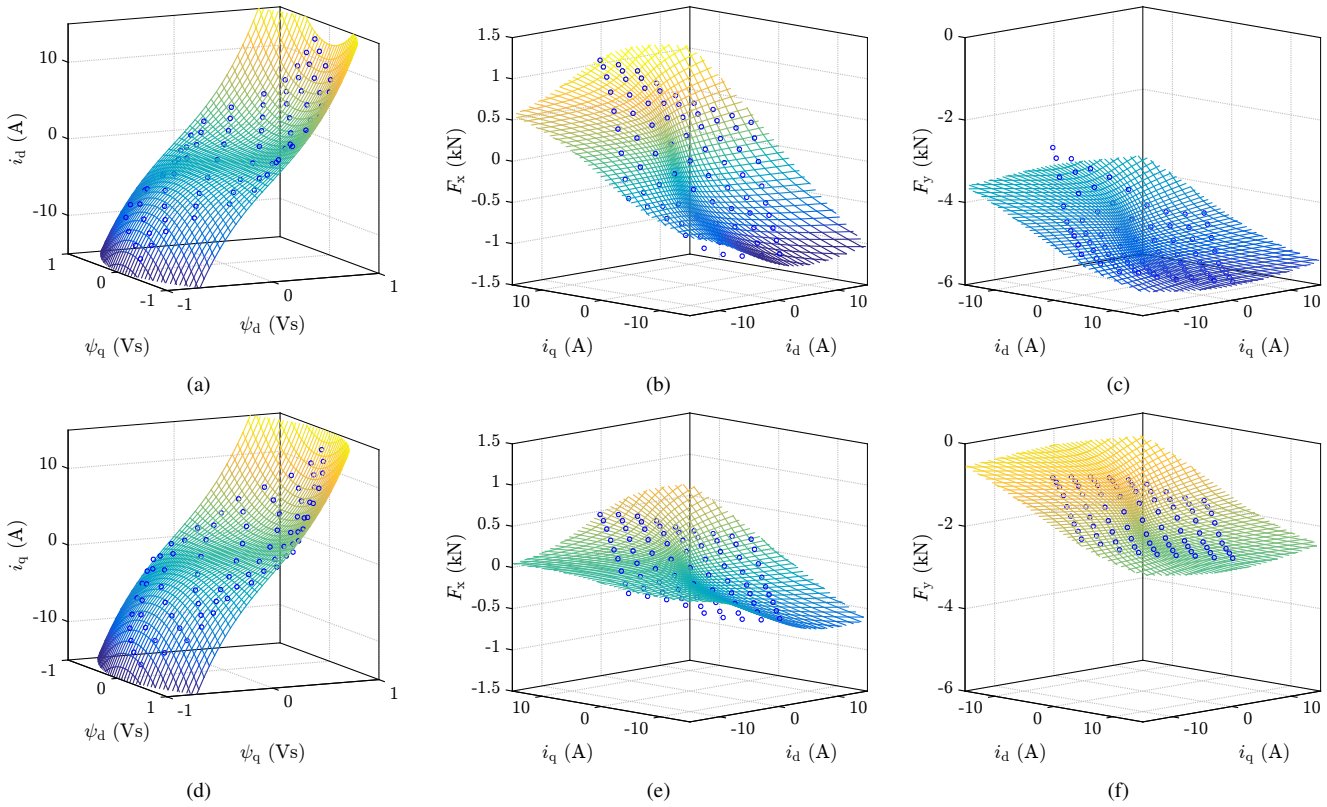

Fig. 7. FEM data represented with blue circles and surfaces showing the model fitting results: (a) $i_{\mathrm{d}}(\psi_{\mathrm{d}}, \psi_{\mathrm{q}})$ at $y = 1.25$ mm; (b) $F_{\mathrm{x}}(i_{\mathrm{d}}, i_{\mathrm{q}})$ at $y = 0.05$ mm; (c) $F_{\mathrm{y}}(i_{\mathrm{d}}, i_{\mathrm{q}})$ at $y = 0.05$ mm; (d) $i_{\mathrm{q}}(\psi_{\mathrm{d}}, \psi_{\mathrm{q}})$ at $y = 1.25$ mm; (e) $F_{\mathrm{x}}(i_{\mathrm{d}}, i_{\mathrm{q}})$ at $y = 2.05$ mm; (f) $F_{\mathrm{y}}(i_{\mathrm{d}}, i_{\mathrm{q}})$ at $y = 2.05$ mm.

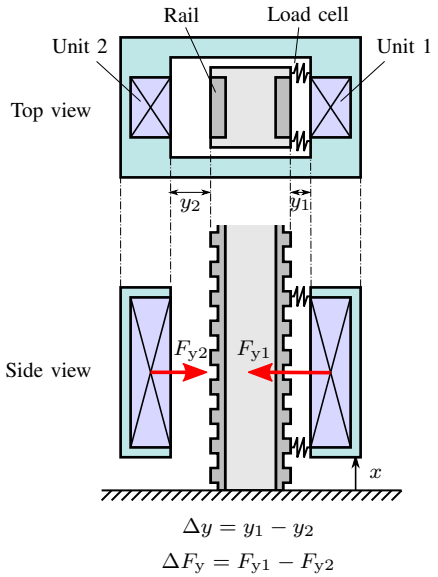

Fig. 8. Experimental configuration for measuring the differential normal force ΔF_{y} of a double-sided bearingless FSPM motor, using four load cells located at each corner of motor unit 1. The differential airgap Δy and the d-axis currents $i_{\mathrm{d1}} = -i_{\mathrm{d2}}$ were varied.

omitted in the model. The inclusion of the both d-axis flux paths in the model is particularly important.

V. Conclusions

The magnetic characteristics of a linear bearingless FSPM machine were analysed. Based on equivalent magnetic models, a set of analytical equations was derived to describe the currents and the force production of the machine. The effects of self-axis magnetic saturation, cross-saturation, and airgap variation were taken into account. The proposed model can be used for real-time control and estimation in bearingless FSPM motor drive systems. The model can be fitted to the measured data or to the data computed using the FEM. An example of the FEM analysis and LLS fitting for a test machine was presented. The validity of the FEM data and the proposed model was verified by measuring the normal forces of a prototype machine.

Acknowledgment

This work was supported in part by the Academy of Finland.

References

[1] E. Hoang, A. H. Ben-Ahmed, and J. Lucidarme, "Switching flux permanent magnet polyphased synchronous machines," in *Proc. 7th Eur. Conf. Power Electronics and Applications (EPE97)*, vol. 3, Trondheim, Norway, Sept. 1997, pp. 903–908.

[2] Z. Q. Zhu, Y. Pang, D. Howe, S. Iwasaki, R. Deodhar, and A. Pride, "Analysis of electromagnetic performance of flux-switching permanent-magnet machines by nonlinear adaptive lumped parameter magnetic circuit model," *IEEE Trans. Magn.*, vol. 41, no. 11, pp. 4277–4288, Nov. 2005.

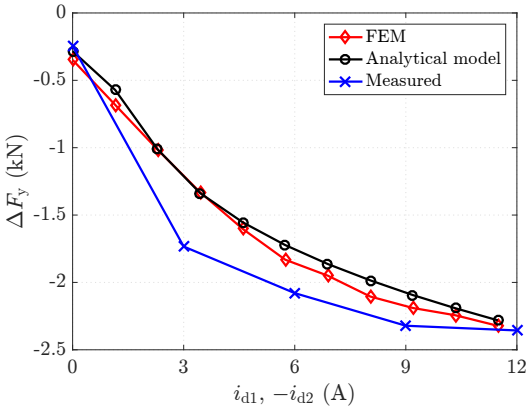

(a) $\Delta y = -0.2$ mm, $i_{d1} = -i_{d2}$

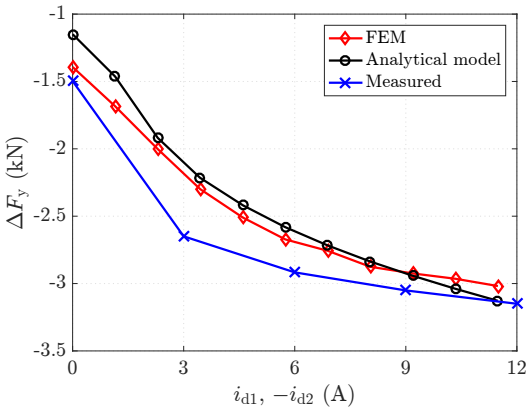

(b) $\Delta y = -0.8$ mm, $i_{d1} = -i_{d2}$

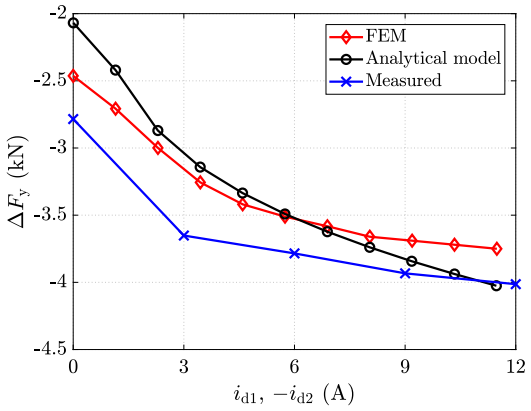

(c) $\Delta y = -1.4$ mm, $i_{d1} = -i_{d2}$

Fig. 9. Measured differential normal force compared with the corresponding FEM-based differential force and the normal force calculated from the fitted model at different d-axis currents: (a) $\Delta y = -0.2$ mm; (b) $\Delta y = -0.8$ mm; and (c) $\Delta y = -1.4$ mm.

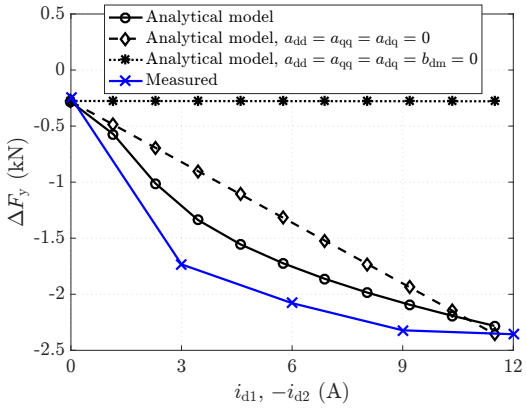

Fig. 10. Differential normal force calculated from the three model fits of Table I at different d-axis currents $i_q = 0$ and $\Delta y = -0.2$ mm.

[3] W. Gruber and K. Radman, "Modeling and realization of a bearingless flux-switching slice motor," *Actuators*, vol. 6, no. 12, Mar. 2017.

[4] C. F. Wang, J. X. Shen, L. L. Wang, and K. Wang, "A novel permanent magnet flux-switching linear motor," in *Proc. IET PEMD*, York, U.K., Apr. 2008, pp. 116–119.

[5] M.-J. Jin, C.-F. Wang, J.-X. Shen, and B. Xia, "A modular permanent-magnet flux-switching linear machine with fault-tolerant capability," *IEEE Trans. Magn.*, vol. 45, no. 8, pp. 3179–3186, Aug. 2009.

[6] L. Huang, H. Yu, M. Hu, J. Zhao, and Z. Cheng, "A novel flux-switching permanent-magnet linear generator for wave energy extraction application," *IEEE Trans. Magn.*, vol. 47, no. 5, pp. 1034–1037, May 2011.

[7] R. Cao, M. Cheng, C. Mi, W. Hua, X. Wang, and W. Zhao, "Modeling of a complementary and modular linear flux-switching permanent magnet motor for urban rail transit applications," *IEEE Trans. Energy Convers.*, vol. 27, no. 2, pp. 489–497, June 2012.

[8] L. Huang, H. Yu, M. Hu, and H. Liu, "Study on a long primary flux-switching permanent magnet linear motor for electromagnetic launch systems," *IEEE Trans. Plasma Sci.*, vol. 41, no. 5, pp. 1138–1144, May 2013.

[9] I. Petrov, T. Purosto, T. Hakala, and J. Ratia, "Electric linear motor," 2016, *Patent Application WO 2016/207136 A1*.

[10] S. Zhou, H. Yu, M. Hu, C. Jiang, and L. H. 1, "Nonlinear equivalent magnetic circuit analysis for linear flux-switching permanent magnet machines," *IEEE Trans. Magn.*, vol. 46, no. 2, pp. 882–886, Feb. 2012.

[11] S. R. Aleksandrov, L. Wang, D. T. E. H. van Casteren, J. J. H. Paulides, and E. A. Lomonova, "Semi-analytical analysis of rotating and linear flux-switching PM machines including skewing," in *Proc. EVER*, Monte Carlo, Monaco, Apr. 2017.

[12] J. Fischer and U. Moser, "Die nachbildung von magnetisierungskurven durch einfache algebraische oder transzendente funktionen," *Archiv für Electrotechnik*, vol. 42, no. 5, pp. 286–299, 1956.

[13] A. E. Fitzgerald, C. Kingsley, Jr., and S. D. Umans, *Electric Machinery*, 6th ed. Boston, MA: McGraw-Hill, 2003.

[14] M. Hinkkanen, P. Pescetto, E. Mölsä, S. E. Saarakkala, G. Pellegrino, and R. Bojoi, "Sensorless self-commissioning of synchronous reluctance motors at standstill without rotor locking," *IEEE Trans. Ind. Appl.*, vol. 53, no. 3, pp. 2120–2129, May/June 2017.

[15] S. E. Saarakkala, M. Sokolov, V. Mukherjee, J. Pippuri, K. Tammi, A. Belahcen, and M. Hinkkanen, "Flux-linkage model including cross-saturation for a bearingless synchronous reluctance motor," in *Proc. 15th International Symposium on Magnetic Bearings (ISMB15)*, Kitakyushu, Japan, Aug. 2016.